Scientific Data

https://doi.org/10.1038/s41597-026-07065-x

Article in Press

"Dense Amygdala": Extensive Complex-valued Functional MRI of the Ventral and Medial Temporal Lobe during Passive Movie Watching in Three Individuals

Received: 30 October 2025

Accepted: 11 March 2026

Cite this article as: Tyszka, J.M., Diamandis, Z., Keles, U. *et al.* "Dense Amygdala": Extensive Complex-valued Functional MRI of the Ventral and Medial Temporal Lobe during Passive Movie Watching in Three Individuals. *Sci Data* (2026). https://doi.org/10.1038/s41597-026-07065-x

J. Michael Tyszka, Zachary Diamandis, Umit Keles, Yue Xu, Na Yeon Kim, Wenying Zhu, Qianying Wu, David A. Kahn & Ralph Adolphs

"Dense Amygdala": Extensive Complex-valued Functional MRI of the Ventral and Medial Temporal Lobe during Passive Movie Watching in Three Individuals

Authors
J. Michael Tyszka[1], Zachary Diamandis[2], Umit Keles[1], Yue Xu[2], Na Yeon Kim[1], Wenying Zhu[1], Qianying Wu[1], David A. Kahn[1,2] and Ralph Adolphs[1,2]

Affiliations
1. Division of Humanities and Social Sciences, California Institute of Technology, Pasadena CA
2. Division of Biology and Bioengineering, California Institute of Technology, Pasadena, CA

Corresponding Author
J. Michael Tyszka
B102A Broad 114-96
1200 E California Blvd
Pasadena, CA 91125, USA
Email: jmt@caltech.edu

Abstract

Dense, individual-level datasets are an important resource for social neuroscience that enable models of brain responses to a wide range of naturalistic features, often investigated with movie fMRI. This data release provides high spatiotemporal resolution 3 Tesla BOLD fMRI data in three healthy participants while viewing four feature-length movies with sound (Grand Budapest Hotel, Forrest Gump, Planet Earth, Jiro Dreams of Sushi; ca. 520 minutes) and a movie trailer composite, together with clip and movie repeats. All movie functional data were acquired with partial brain coverage from an approximately axial slab covering ventral prefrontal and temporal lobes, including the amygdala, with a repetition time of 556 ms and complex-valued image reconstruction. The dataset is released in both unprocessed and minimally preprocessed forms with individual, high quality anatomic templates. Preprocessed fMRI data are provided in both individual template and *FreeSurfer* average surface spaces. Reference raw data are provided for a conventional face-object functional localizer task. Auxiliary physiological data includes 4-lead ECG waveforms, image-estimated respiratory waveforms and pupillometry. Quality metrics include temporal SNFR maps, high-resolution B_0 maps, EPI dropout and head motion parameters for all runs. Physiological noise estimation and cleaning used spatial independent component analysis and custom, per-subject component classification. Annotations for the movies provide automated low-level audiovisual and facial features, as well as emotion ratings from each participant. The presence of presumed BOLD neurovascular responses not associated with physiological or instrumentation noise was confirmed using temporally concatenated spatial independent component analysis (tcsICA).

Background and Summary

This dataset is a product of ongoing studies of social cognition in humans, with a particular focus on the role of the amygdala in emotion and its response to naturalistic emotional and social stimuli such as movies. Rich audiovisual stimuli evoke a complex and nuanced set of responses in the human brain and are a valuable bridge between earlier resting-state and task-based fMRI experiments, particularly for social cognition[1,2]

While traditional large-sample group analyses can identify broad patterns with high sensitivity, they can obscure meaningful individual differences in brain organization and network topology[3,4] and can blur distinctions between functionally distinct areas[4]. In contrast, acquiring extensive within-subject data can greatly improve estimates of individual responses and the identification of unique neurovascular responses often lost in inter-subject averaging[3–6]. This is particularly relevant for studying regions like the amygdala, where processing related to stimulus salience may exhibit significant inter-individual variation [7–10]. Precision imaging has so far focused on cortex, generally with a whole-brain field-of-view and has not aimed to optimize signal in the amygdala, which was a key motivation for the present study.

To probe brain function effectively within individuals, naturalistic paradigms like movie-watching fMRI (movie-fMRI) offer several advantages over traditional task-based approaches[1]. First, the number and diversity of stimuli available is enormous, allowing for intelligent sampling of the videos to be used in a specific experimental paradigm. Second, movies elicit remarkably strong and reliable responses across participants' brains[11,12]. Third, they are highly engaging and immersive[13,14], and by design depict real-world events, often eliciting strong emotions[15]. Finally, movie-fMRI is ideal for studying social and emotional processing, since movies generally emphasize complex cognitive and social features in more realistic contexts[13]. Several valuable movie-fMRI datasets have been released previously, including the Study Forrest project[16], Grand Budapest Hotel data release[17], the Emo-FilM dataset[18], and the Naturalistic Neuroimaging Database[19].

The dataset presented here consists of dense, precision neuroimaging at the individual level[20], with over ten hours of complex-valued BOLD fMRI data for each of three subjects . To achieve a high temporal resolution (556 ms), image coverage was limited to an approximately transverse slab through ventral brain centered around the amygdala and including ventral frontal and temporal cortices. Audiovisual stimuli include one very-well characterized movie ("Forrest Gump)"[16,21,22], one movie with previously released fMRI data ("The Grand Budapest Hotel")[17,23,24], two episodes from a previously unstudied natural history documentary ("Planet Earth"), an unstudied documentary film ("Jiro Dreams of Sushi)" and a short composite of three movie trailers.

Structural and both minimally preprocessed and physiologically denoised functional MRI data are organized in BIDS format and are provided with quality metrics in both individual volumetric and a standard surface space. We use a standard structural analysis pipeline, *FreeSurfer* [25], for cortical surface estimation and a custom volumetric functional preprocessing pipeline employing state-of-the-art functions from *fMRIPrep* [26] and *SDCflows* [27]. All data were collected at the Caltech Brain Imaging Center on the same MRI system with no operating or pulse sequence software changes.

The dataset is distinguished by the following features: (1) All functional MRI data is complex-valued and acquired at a sub-second temporal resolution allowing for more specific isolation of physiological noise, particularly from breathing, and the identification of venous signal. (2) the fMRI acquisition sequence is optimized for maximum signal in the ventral and medial temporal lobe (3) the dataset includes a significant amount of naturalistic, movie-fMRI data per participant – including various repeated stimuli - facilitating robust intra-subject analysis, (4) the stimuli are diverse, spanning a broad space of features hypothesized to activate the amygdala, (5) high-quality, individual anatomic templates are included. Taken together, these features aim to provide a dataset that can address scientific questions focused on the human ventral visual stream and amygdala in social neuroscience.

Finally, we use the term "neurovascular" when referring to presumed BOLD neurovascular responses not associated with physiological or systematic noise, respecting the usual caveat that the BOLD hemodynamic response in the brain is a complex and indirect surrogate for underlying neural dynamics[28–30].

Methods

Participants and Ethics Statement

Three healthy adult participants were recruited and provided written informed consent under protocols IR21-1176 and IR24-1490 approved by the Caltech Institutional Review Board (IRB). All methods were carried out in accordance with US Federal Policy for the Protection of Human Subjects codified in Department of Health and Human Services' regulations 45 CFR Part 46. Participant ID, sex and age in years were as follows: Damy001, Male, 59; Damy002, Female, 25; Damy003, Male, 56. All participants consented to open data sharing, and the deidentified data is released under a Creative Commons Zero (CC0) license.

MRI Data Acquisition

All MRI data were acquired using a 3T whole-body MRI system (Prisma.Fit, Siemens Medical Solutions, Malvern, PA) maintained by the Caltech Brain Imaging Center with a 32-channel head receive array coil. Imaging sequence parameters are summarized in Table 1.

Purpose	Sequence	Dimensionality / Coverage	TR (ms)	TE (ms)	TI (ms)	Flip (deg)	Accel (R x M)	Voxel (mm)
Structural	T1w MEMP-RAGE	3D / WB	2.6	1.6	1150		2 x 1	0.9
Structural	T2w SPACE	3D / WB	3200	564	-		2 x 1	0.9
Movie Viewing								
Functional	T2*w GRE-EPI	2D multislice / slab	556	30	-		2 x 4	2.0
Fieldmap	T2w SE-EPI	2D multislice / slab	2769	53	-		2 x 1	2.0
Face Localizer								
Functional	T2*w GRE-EPI	2D multislice / WB	1000	30	-		1 x 5	2.0
Fieldmap	T2w SE-EPI	2D multislice / WB	5500	48	-		1 x 1	2.0

Table 1: *Structural and functional imaging sequence parameters. All voxels have isotropic dimensions, and all EPI data was complex-valued. All voxel sizes are isotropic and complete imaging parameters are provided as BIDS metadata in the OpenNeuro ds006947 repository. Abbreviations: WB – whole-brain, R - in-plane GRAPPA acceleration factor, M - multiband slice acceleration factor.*

Structural Magnetic Resonance Imaging: T1-weighted (T1w) and T2-weighted (T2w) images were acquired in all 12 imaging sessions. T1w 3D structural images with a 0.9 mm isotropic voxel size were acquired using a multi-echo magnetization-prepared RAGE (MEMP-RAGE) sequence with magnitude RMS combined-echo image reconstruction (Figure 1a). T2w 3D structural images with a 0.9 mm isotropic voxel size were acquired using a Siemens proprietary turbo spin echo sequence (SPACE) with magnitude reconstruction (Figure 1b).

Functional Magnetic Resonance Imaging: Complex-valued partial brain coverage BOLD fMRI data during movie viewing were acquired in all participants and sessions. BOLD movie-viewing fMRI were acquired using a 2.0 mm isotropic T2*-weighted EPI with an in-plane GRAPPA acceleration, R = 2 and slice acceleration, M = 4 (CMRR, University of Minnesota) (Figure 1c, k). An additional single-band reference image was generated for each multiband series for use as an intermediate high-contrast registration reference (Figure 1d). Single-band phase-encoding polarity-reversed (PEPOLAR) SE-EPI image pairs were acquired for EPI distortion correction immediately before each functional run, with identical slice geometry and EPI echo spacing to the BOLD EPI series (Figure 1e, l).

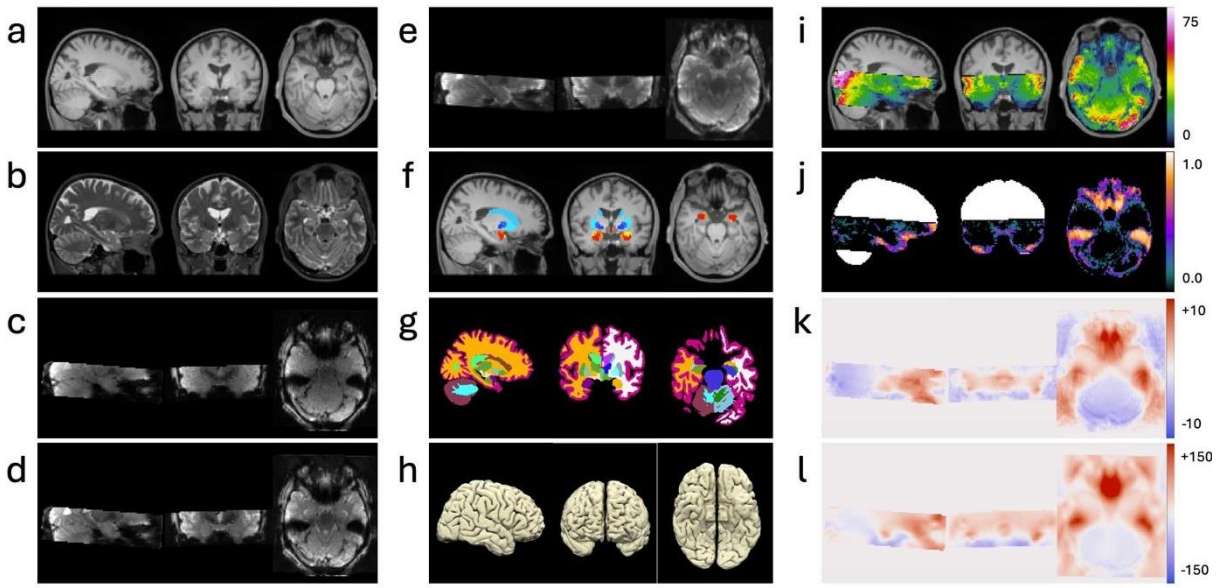

Figure 1: *Preprocessed structural and functional MRI data including (a) T1w MEMP-RAGE, (b) T2w SPACE, (c) T2*w multi-band and (d) single-band reference BOLD EPI magnitude images (e) T2w SE-EPI magnitude reference (f) CIT168 subcortical labels (g) Freesurfer automatic segmentation (aseg) tissue labels (h) Freesurfer native-space pial surface, (i) mean temporal SFNR map (dimensionless ratio), (j) estimated T2*w fractional signal dropout map (dimensionless ratio) (k) BOLD EPI temporal complex-difference phase images (radians) and (l) TOPUP estimated B_0 offset (Hz). All images and surfaces are shown in the individual structural template space.*

A one-back categorical image task was used as a functional reference for ventral temporal cortical and amygdala responses to categorial image presentation. The participant viewed images of faces, objects, buildings, and scrambled objects presented in 15 s blocks of the same category with 1 s image presentation time. Each set of four category blocks was preceded by 15 s of central fixation and repeated four times with category order counterbalancing for a total of 300 s. BOLD fMRI acquisitions for this task had whole brain coverage with 2.5 mm isotropic voxels and a TR of 1000 ms (Table 1). Functional localizer imaging data and events metadata are provided for each participant in a separate session folder but without preprocessing.

Audiovisual Stimuli

We selected our stimuli based on two primary criteria: 1. links to other studies and databases that used movie-fMRI, and 2. hypothesized importance of movie features to amygdala activation. With respect to continuity with prior movie-fMRI work, Forrest Gump[16,21,22] and Grand Budapest hotel[17,24,31] had been previously used, and were chosen for that reason. With respect to features hypothesized to activate the amygdala, this structure has long been implicated in both conscious[32] and non-conscious[33] responses to food in human neuroimaging studies, consistent with its role in food consumption from recordings in rodents[34]. For this reason, we chose the documentary "Jiro Dreams of Sushi," given the additional relevance that our three participants were all very familiar with, and fond of sushi. Finally, we sought to also include visual features found in nature, in

particular showing animals, since our own prior work of single-unit recordings from the human amygdala had shown strong responses to animals[35]. All these features are also broadly consistent with the amygdala's generally acknowledged role in saliency representation, thought to be the abstract stimulus features that engage this structure's modulation of attention, memory, and decision-making.

Stimulus presentation and response capture were performed using an LCD back-projection system and optical response button box (Current Designs Inc., Philadelphia, PA) controlled via scripts running in Psychophysics Toolbox 3[36]. Stimuli consisted of full presentations (with partial repeats) of the feature-length movies "Forrest Gump," (Blu-ray EAN: 4010884250916 © 1994, 2011 Paramount Pictures) and "Grand Budapest Hotel" (Blu-ray Catalog #2289743 © 2014 Twentieth Century Fox Film Corporation) the documentary "Jiro Dreams of Sushi" (Blu-ray Catalog #10474 © 2012 Magnolia Home Entertainment) and episodes from the nature documentary "Planet Earth" (Blu-ray Disc ISBN 1-4198-5180-2 © 2007 BBC Worldwide Ltd) distributed across twelve imaging sessions. Audiovisual stimuli for "Forrest Gump", "Grand Budapest Hotel", "Jiro Dreams of Sushi" and "Planet Earth" were derived from purchased commercial BlueRay® media. Full-length movies were divided at natural scene changes into segments ranging from approximately 5 to 20 minutes in length with approximately 5 seconds of overlap. Segments for "Forrest Gump" were identical to those used in the StudyForrest project[16,37]. Three commercial movie trailers: "Everything Everywhere All at Once", © 2022, A24 Films[38], "Big Gold Brick", © 2022, Samuel Goldwin Films[39] and "Warning", © 2021 Lionsgate[40] were chosen for dense social and emotional content and composited into a single 5 minute video that contained a large diversity of rapidly presented features. Additionally, participants viewed twelve total repetitions of selected movie trailers, and each session included a single repetition of the first five minutes of the first video segment of the previous session's movie, totaling an additional twelve repeated segments. This structured selection aims to support detailed investigation of neural processing in response to both familiar and novel emotionally and socially relevant content.

All video and audio preprocessing was performed using *FFmpeg* 6.1.1[41]. All video stimuli were resampled to a frame size of 1280 x 720 at 30 frames-per-second (FPS) for display. Audio tracks were extracted and compression filtered to improve performance in the presence of background scanner noise. Video source information, exact segment cut timings, video preprocessing scripts and stimulus presentation code are provided in the accompanying data release GitHub repository (https://github.com/adolphslab/DenseAmygdalaRelease).

All stimulus presentation and experimental control was implemented using *PsychoPy* (v2021.2.3) running on a Windows 7 workstation. Video stimuli were presented using a rear-projection system employing a commercial LCD projector (IN5180, InFocus Corporation, Tigard, OR) with an approximate eye-to-screen distance of 100 cm and displayed width of 38 cm (28.8° horizontal visual angle).

All participants wore MR-compatible earbuds (SR14, Sensimetrics Corporation, Gloucester, MA) embedded in individually molded foam earplugs (CEP001-O, Radians Inc., Memphis, TN) that were adjusted for each of our three participants. Additional sound suppression was provided by over-ear muffs (Razor Slim Passive, Walker's Game Ear, Irving Texas) modified for MR-compatibility and to

fit within the head coil. Earbud volume levels were adjusted with participant feedback prior to each run using an audio-only clip played during 30 s of the same EPI sequence used for data acquisition.

Eye Tracking Data Acquisition

Pupil size and gaze position were recorded concurrently with fMRI during every passive movie-watching run using a remote, MR-compatible infrared eye-tracker (EyeLink 1000+, SR Research, Ontario, Canada) positioned at the rear of the bore. Eye tracking data acquisition was controlled by the stimulus script resulting in frame-accurate synchronization with the stimulus presentation. Before each run, a nine-point calibration followed by validation was performed and a validation accuracy image was retained. Pupil size and gaze position were sampled at 500 Hz. All participants had natural or contact lens-corrected visual acuity of 20/20 at the time of the experiment confirmed by Snellen Chart.

After data collection, gaze position traces were overlaid onto corresponding movie frames to visually assess spatial accuracy. This inspection revealed that gaze positions frequently failed to track visually salient scene elements such as the face of a speaking character or other prominent objects, consistent with suboptimal gaze-to-screen mapping accuracy and/or calibration drift under the in-bore recording conditions. In video-based eye tracking, gaze position is derived from image-based eye features (typically the pupil center relative to a corneal reflection/glint) and then mapped to screen coordinates via the calibration model; this mapping can degrade with small changes in head position, camera geometry, or calibration drift across time. By contrast, pupil size is estimated directly from the pupil boundary/ellipse fit in the eye-camera image and does not rely on the gaze calibration transform. Therefore, even when absolute gaze coordinates are unreliable, the pupil size time series can remain usable if pupil segmentation is stable (see Pupillometry Data Quality). Given these reliability concerns for gaze position, gaze traces are excluded from this release. Instead, only the continuously recorded raw pupil size data are provided in BIDS-compatible format. Pupil size remains valuable for indexing arousal and cognitive load, and for nuisance-regressing arousal-related and physiological confounds.

Behavioral Questionnaires

Six questionnaires assessing participants' psychologically relevant state were collected after each session. The questionnaires include the following information: Day of Visit (sleep hours, wakefulness), Video Ratings (subjective enjoyment and engagement) and Standard Questionnaires used in psychological assessment (BDI-2[42], STAI-state[43], PANAS[44], PSS[45]) and are included in the OpenNeuro ds006947 repository as a BIDS-format phenotype file. Participants did not indicate elevated levels of depression, state anxiety or stress at any timepoint [42,43,45]. For all participants, negative affect was within normal limits at all timepoints, as was positive affect for two participants. However, participant Damy002 endorsed extremely low levels of positive affect at 10 timepoints[46]. We acknowledge that deep phenotyping results such as this may affect responses and in turn, the interpretability of the data. Additional emotion ratings were also obtained throughout subsequent out-of-scanner viewing of all movies; see Manual Emotional Features below.

Video Feature Labeling

To facilitate analyses of the brain activations evoked by specific movie content, we extracted a set of features from the video stimuli using our open-source Python library (https://github.com/ukeles/VidFeatureXtract), including low-level audiovisual features that capture basic sensory dynamics and face features that quantify the presence and size of faces.

Temporal sampling and alignment. All features were computed at the native frame rate of each stimulus. Presentation timestamps (PTS, seconds) were read from the video stream using the PyAV library (https://github.com/PyAV-Org/PyAV) and stored per video to enable precise downstream alignment to the fMRI TR.

Audio features. We de-multiplexed (demuxed) the audio track from each video with *MoviePy* (https://zulko.github.io/moviepy) and *FFmpeg* (without resampling) and computed four time-varying features on a frame-by-frame basis using the *librosa* library . Short-time analysis used a window size of 2048 samples and a hop length of 512 samples. The features were: (i) root-mean-square (RMS) amplitude, providing a measure of signal power; (ii) zero-crossing rate (ZCR), the rate at which the signal changes sign; (iii) peak envelope, the peak amplitude of the signal within each frame on a decibel scale; and (iv) total energy, the sum of squares of the signal within each frame on a decibel scale. These four features were concatenated into a single time series, providing a compact representation of each video's audio.

Visual features. To quantify basic visual content, we computed the spatial mean of pixel values within each video frame across seven channels. Each frame was converted to RGB, HSV (hue, saturation, value), and CIELAB color spaces. We then calculated the mean value for the R, G, B, H, S, V channels and the L (luminance) channel from CIELAB, yielding a 7-dimensional feature vector for each frame.

Face Features. To enable analyses related to social cognition and attention, we performed face detection on every frame of the videos using the *InsightFace buffalo_l* model[47]. For each detected face, the model returned: (i) a bounding box specifying the location and size of the face, (ii) a confidence score indicating detection certainty, and (iii) five 2D facial landmarks (left/right eye, nose, left/right mouth corners). From these outputs, we generated a frame-by-frame time series summarizing three higher-level features: (i) face count, the total number of faces detected in the frame (confidence > 0.5); (ii) total face area, the proportion of the frame occupied by faces; and (iii) average face area, the mean size of detected faces as a proportion of total frame pixels. These features quantify not only the presence of faces but also their size and number, supporting detailed face regressors for fMRI analysis (see Figure 4 below).

The final 4-dimensional audio, 7-dimensional visual, and 3-dimensional face feature time series were then converted and stored in BIDS format.

Manual Emotion Features: Each of the three participants was asked to re-view all full-length video clips out of the scanner in the original presentation order using *Pavlovia* for both video presentation and rating capture. Three commonly used emotional ratings - valence (bivariate), arousal and anxiety - were captured. Every 30 seconds, and at the end of each movie segment,

participants were asked to rate their subjective average experience of these emotion features over the previous 30 seconds. Valence was rated from –5 to +5, while arousal and anxiety were rated from 0 to +5. Individual participant ratings are provided as behavioral tab-separated text (TSV) files.

Data Preprocessing

Individual anatomic template construction: T1w and T2w anatomical images were acquired for each session, resulting in 12 images of each contrast for each participant. Individual minimum deformation structural templates were constructed by iterative non-linear registration of all T1w and T2w images using a multivariate template script from the *ANTs* 2.25 package (*antsMultivariateTemplateConstruction2.sh*)[48]. T1w and T2w individual templates were AC-PC aligned by rigid body registration to the MNI152 2009c nonlinear asymmetric space. Subcortical region labels from the CIT168 atlas were registered to each individual template space using symmetric normalization (SyN) diffeomorphic registration implemented in *ANTs*[49]. All three individual templates with probabilistic subcortical labels were converted to *templateflow* format [REF] prior to integration with the preprocessing pipeline.

FreeSurfer segmentation and cortical parcellation: Whole-brain tissue segmentation, cortical surface estimation and cortical parcellation were performed using FreeSurfer version 7.2 (http://surfer.nmr.mgh.harvard.edu/)[50]. Processing included motion correction and averaging of volumetric T1w images, removal of non-brain tissue, automated Talairach transformation, segmentation of the subcortical white matter and deep gray matter volumetric structures, intensity normalization, tessellation of the gray matter-white matter boundary, automated topology correction [51], and surface deformation following intensity gradients for optimal tissue boundary placement (Figure 1g, h).

Functional data preprocessing: Both structural and functional MRI data were minimally preprocessed using *slabpreproc* (https://github.com/adolphslab/slabpreproc), which is based on *nipype* 1.8.4[52], *sdcflows* 24.0.0[27] and *fMRIPrep* 24.2.0[26]. The processing steps for partial brain functional MRI data are summarized below, with specific software noted in italics. The *slabpreproc* pipeline implements many of the standard practices seen in *fMRIPrep*, such as single-shot resampling from the warped EPI to individual template space but is tailored for slab-selective partial brain coverage since *fMRIPrep* is optimized at various points for whole-brain data. Slice timing correction was omitted due to the short TR (556 ms) consistent with the Human Connectome Project preprocessing approach[53]. Head motion correction used *FSL MCFLIRT* and rigid body transformations were converted to ITK format for later one-shot resampling. Susceptibility distortion corrections were estimated from the polarity-reversed SE-EPI images acquired immediately after each BOLD functional run using FSL *TOPUP* . Registration of the raw, distorted EPI space to the participant's structural template space was performed for each BOLD series as follows: 1. The rigid body transform was estimated mapping the single-band reference (SBRef) image to the distorted SE-EPI with the same phase encoding direction. 2. The distortion-corrected mean SE-EPI image was rigid-body registered to the session level T2w structural image, which in turn was registered to the participant's T2w mid-space template. 3. The composite transform including per-volume head motion correction and susceptibility distortion correction

was constructed and applied to each volume of the BOLD time-series with Lanczos-filtered sinc resampling, resulting in distortion and head motion corrected complex-valued BOLD timeseries images in individual template space. Phase-channel BOLD images were additionally phase unwrapped temporally by complex division by the first image in the time series, prior to spatial resampling.

Key quality control images were estimated from the preprocessed T2*w BOLD EPI and SE-EPI data for each task series. Temporal signal-to-fluctuation-noise (fSFNR) maps[54] following temporal demeaning were estimated using the *nipype TSNR* interface, B_0 field offset maps were generated by *TOPUP* and signal dropout maps derived independently. Signal dropout, *D,* was estimated using Equation (1)

$$D(x,y,z) = 1 - \frac{\hat{S}_{sbref}(x,y,z)}{\hat{S}_{seepi}(x,y,z)} \quad (1)$$

where $\hat{S}_{sbref}(x,y,z)$ and $\hat{S}_{seepi}(x,y,z)$ are the SBRef and mean SE-EPI images following normalization the median brain signal at voxel (x, y, z), resulting in voxel-wise dropout estimates of 1.0 for complete signal dropout (no signal in the SBRef image) and 0.0 for complete signal preservation. Dropout estimates were clamped to the range [0, 1].

Inspection of the phase channel of the BOLD EPI time series reveals a strong time-varying phase evolution within the brain consistent with the respiratory cycle, with a period of 3 to 10 seconds. Work by other groups has established that this phase time-course is a useful proxy for an independently acquired respiratory transducer waveform. Proxy respiration waveforms were generated for all BOLD series from the median of the temporally unwrapped phase channel within the brain mask using the *PhaseRespWave* class of the *mriphysio* python package (see Code Availability below).

Finally, a PDF summary report was generated for each BOLD series including head motion correction results, structural template sections, resampled EPI images in template space and quality control images including tSFNR, B_0 offset, signal dropout.

Preprocessing scripts are provided in the code folder of the OpenNeuro ds006947 repository[55]. The *slabpreproc* preprocessing pipeline is available as a GitHub repository (see Code Availability below).

Physiological Denoising of fMRI Data

MELODIC spatial ICA was performed following preprocessing. Individual task acquisitions were divided into movie segments ("long" runs) and 5-minute trailer and movie repeats ("short" runs). An IC classification training set for ICA-FIX consisting of 60 ICAs was drawn randomly from all available movie watching series (30 long and 30 short runs). Five raters manually classified 2 short and two long runs from the training set with no overlap of rated ICAs between raters for a total of 4552 manual IC classifications and a mean of 1517 ICs classified per participant. All raters were trained and classification consistency measured post-training and prior to classification assignments used for ICA-FIX training. For training validation, the remaining 81 ICAs (4441 ICs)

were classified automatically using ICA-FIX trained on the manually classified ICAs. Finally, all runs were automatically denoised using the trained ICA-FIX classifier. We note that the ICA-FIX component classifier was trained on data from an earlier version of *slabpreproc* which used sequential resampling rather than the current single-step resampling from raw EPI to target output spacebut with all other imaging parameters, system specifications and the participant group held constant. The impact of the difference in resampling strategy on FIX classification accuracy is detailed in the Supplementary Information. Overall, the FIX classifier trained on an older pipeline but used on the release data had a high accuracy (~95%, "ground truth" manual classification), but was more conservative than the human rater when labeling components as noise. Both uncleaned and cleaned runs are available in the released dataset for completeness

Data Record

This dataset is made available under a Creative Commons Zero (CC0) license through the OpenNeuro data sharing platform as ds006947[55]. The dataset complies with the Brain Imaging Data Structure (BIDS version 1.10.0) which organizes compressed Nifti-1 format imaging data using a simple folder structure with nested files, each with standardized filenames identifying the type of scan. Metadata are provided according to the BIDS specification in accompanying JSON files ("sidecars"). For each participant, functional and structural MRI, physiological and behavioral data were acquired in 12 x 90-minute scanning sessions over the course of 10 weeks and the repeat of the entire set of Forrest Gump movie segments in two sessions approximately 32 months later (Table 2). Low-level audiovisual features were derived from the as-presented videos. Respiration waveforms were estimated from the fMRI phase channel. Heart rate, respiratory rate and pupil area time series are provided as BIDS-format TSV files for each session and task. T1w and T2w structural images are irreversibly de-identified using the *voxface* customization of *pydeface (*see Code Availability below*)*.

Data Type	Count Per Session	Total Count	Total Duration (mins)
Primary Data			
Structural MRI	T1w and T2w	12 each	-
Movie Segment fMRI	2	24	513
Movie Clip Repeat fMRI	1	12	60
Forrest Gump Repeat fMRI	4	8	
Trailer fMRI	1	12	60
ECG	4	48	633
Pupilometry	4	48	633
Post-scan questionnaires	6	72	-
Derived Data			
Low level audiovisual features	4	48	633
Respiration waveform	4	48	633

Table 2: *Imaging, physiology and behavioral data acquisition overview for each participant. Data was acquired in 12 experimental sessions. The Movie Clip Repeat refers to the presentation of a 5 minute clip of a movie segment from the previous session. The Forrest Gump Repeat refers to the repeat presentation in two sessions of the entire set of Forrest Gump movie segments. All fMRI data are complex-valued. Post-scan questionnaires included BDI-2, STAI, PANAS, PSS, sleep and wakefulness.*

Technical Validation

Presence of Stimulus-Evoked BOLD Responses

Preliminary characterization of task-evoked BOLD responses used temporally concatenated spatial Independent Component Analysis (tcsICA)[56] of the complex-valued video-watching data for each participant over all sessions and runs. The magnitude and phase channels were analyzed independently to isolate spatially correlated patterns of BOLD activity. All 4D BOLD images without ICA-FIX physiological denoising were preprocessed for tcsICA as follows: 1. Construction of a grand signal mask for each participant across all available tasks. The estimated signal dropout masks were thresholded at a fractional dropout < 0.75 and combined over all tasks by logical AND before final masking with the individual brain mask ($p > 0.75$) to create a grand signal mask for tcsICA computation. 2. High-pass temporal filtering ($f > 0.005$ Hz) and isotropic Gaussian spatial smoothing (FWHM = 1 mm). All tcsICA was performed using *FSL melodic* (version 3.15) with Incremental Group PCA (MIGP) disabled to preserve the temporal mode for each component, with target dimensionality estimated automatically for the magnitude channel tcsICA and fixed at 50 for the phase channel tcsICA.

ICs were classified by inspection into neurovascular (Figure 2a, b), cardiac and mixed cardiorespiratory (Figure 2c) and other components including gross head motion, venous sinus and CSF-localized signal, imaging artifacts and unclassified noise sources. For the magnitude channel tcsICA, the short TR of the functional runs allowed separation of respiratory and aliased cardiac components in all three participants. The Nyquist frequency for a TR of 0.556 s is 0.9 Hz, so aliased pulsatile cardiac components are observed in the 0.4 Hz to 0.7 Hz band (Figure 2c), corresponding to an unaliased band between 1.1 and 1.4 Hz (66 to 84 bpm). Some independent components (ICs) displayed mixed cardiac and respiratory power spectrum components but are grouped with cardiac components below. The breakdown of magnitude channel IC count and total percent explained variance by IC class for each participant is shown in Table 3.

	IC Count				Explained Variance (%)			
Participant	Neuro-vascular	Cardiac	Other	Total	Neuro-vascular	Cardiac	Other	Total
Damy001	12	35	31	78	17.7	41.4	40.9	100.0
Damy002	19	37	26	82	27.4	39.6	32.9	100.0
Damy003	13	27	26	66	23.0	36.4	40.6	100.0

Table 3: *Summary of temporally concatenated spatial ICA of the magnitude channel images over all video sessions and runs for each participant. Between 12 and 19 neurovascular components were identified for each participant with most non-neurovascular components arising from cardiac and cardiorespiratory sources based on the temporal mode power spectrum.* The Other class consists of ICs associated with gross motion, venous sinuses, CSF spaces, imaging artifacts or unclassified noise sources. *Neurovascular components contributed between approximately 18% and 27% of the total explained variance, with cardiac/cardiorespiratory components accounting for approximately 40% of the total.*

For the phase-channel of the functional runs, the tcsICA with 50 components of the temporally unwrapped phase revealed a dominant respiratory component in the 0.1 to 0.3 Hz band, with the remaining components classified from their temporal modes as arising primarily from head motion. Phase channel ICs were dominated by respiratory components in the 0.1 and 0.3 Hz band (Figure 2d).

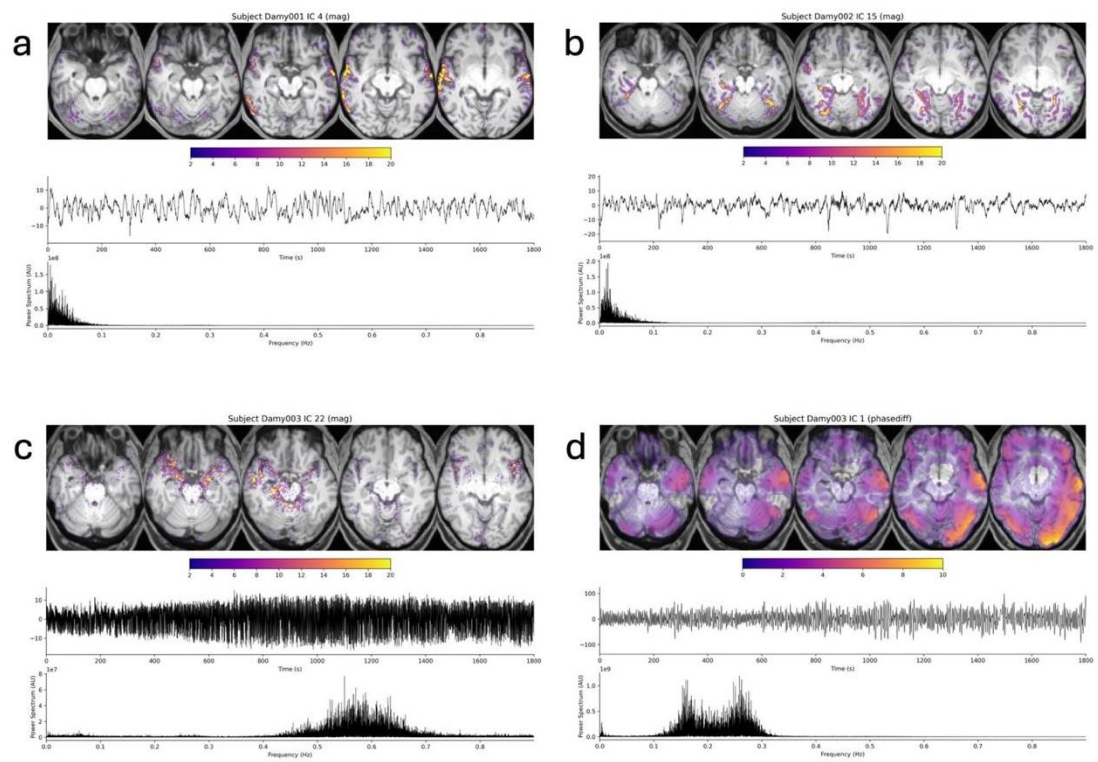

Figure 2: Representative spatial independent components classified as (a) early auditory (b) ventral visual (c) cardiovascular and (d) respiratory in origin. (a)-(c) were isolated from a temporally concatenated spatial ICA (tcsICA) of the magnitude images over all BOLD series for participants Damy001, Damy002 and Damy003 respectively. (d) The dominant component isolated from a tcsICA of the temporally unwrapped phase images over all BOLD series for Damy003. For each independent component, the top row shows the mixture model z-score for the component weights overlayed on T1w anatomy, the middle row shows the first 1800 s of the temporal mode of the

component, and the bottom row shows the power spectrum of the entire temporal mode on a frequency scale normalized to the Nyquist frequency.

To gauge the spatial coverage of neurovascular ICs within the imaged slab, masks were generated from the thresholded mixture model output of FSL *melodic* for each IC. These masks represent voxels in each IC for which the signal contribution exceeded the noise contribution (mixture threshold 0.5). A map of the number of suprathreshold ICs at a given voxel location was then constructed by simple summation of all masks for each participant (Figure 3a). Similarly, a count of the number of suprathreshold voxels within the bilateral amygdala mask ($p > 0.25$) for each IC, IC class and participant can be used as an estimate of the neurovascular BOLD signal present in this data within the amygdala (Figure 3b). Individual differences in amygdala-localized neurovascular responses are apparent, with Damy002 demonstrating greater neuronal IC contributions within the amygdala than either Damy001 or Damy003.

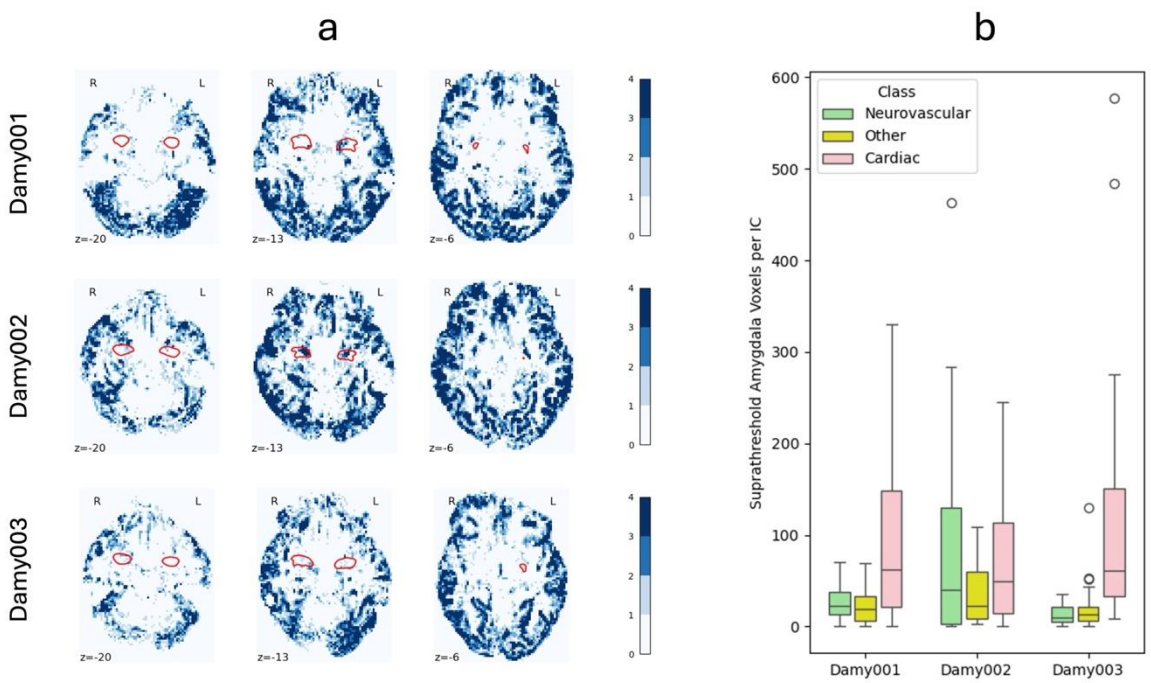

Figure 3: Brain coverage by neurovascular ICs for each participant. (a) The number of ICs with a mixture model z-score that exceeds threshold at each voxel. The boundary of the amygdala is shown in red ($p > 0.25$ in the individual probabilistic atlas). (b) The distribution of the per-IC count of suprathreshold voxels within the amygdala for each IC class and participant. The Other class consists of ICs manually classified as arising from gross motion, large venous sinuses, CSF spaces, image artifacts or unclassified noise sources.

An additional model-driven confirmation of task-evoked BOLD responses in the movie-watching data was performed using conventional univariate general linear modeling of face feature responses. For the movie data, a GLM was constructed from the face area and total number of faces

(see Video Feature Labeling above), with derived temporal derivative and dispersion, high pass cosine filtering and SPM HRF convolution, implemented in *nilearn* . For comparison, a single run of a blocked design multimodal face-object-body-scrambled localizer task was acquired for each participant with whole-brain coverage and preprocessed with *fMRIPrep*. The z-scored regression coefficients for both models were resampled to the *fsaverage* surface space for visual comparison using *nilearn*. Individual variations in ventral temporal cortical face-selective responses were apparent, as were similarities in spatial extent and interhemispheric asymmetries of responses within each participant between the movie and face localizer evoked activations (Figure 4).

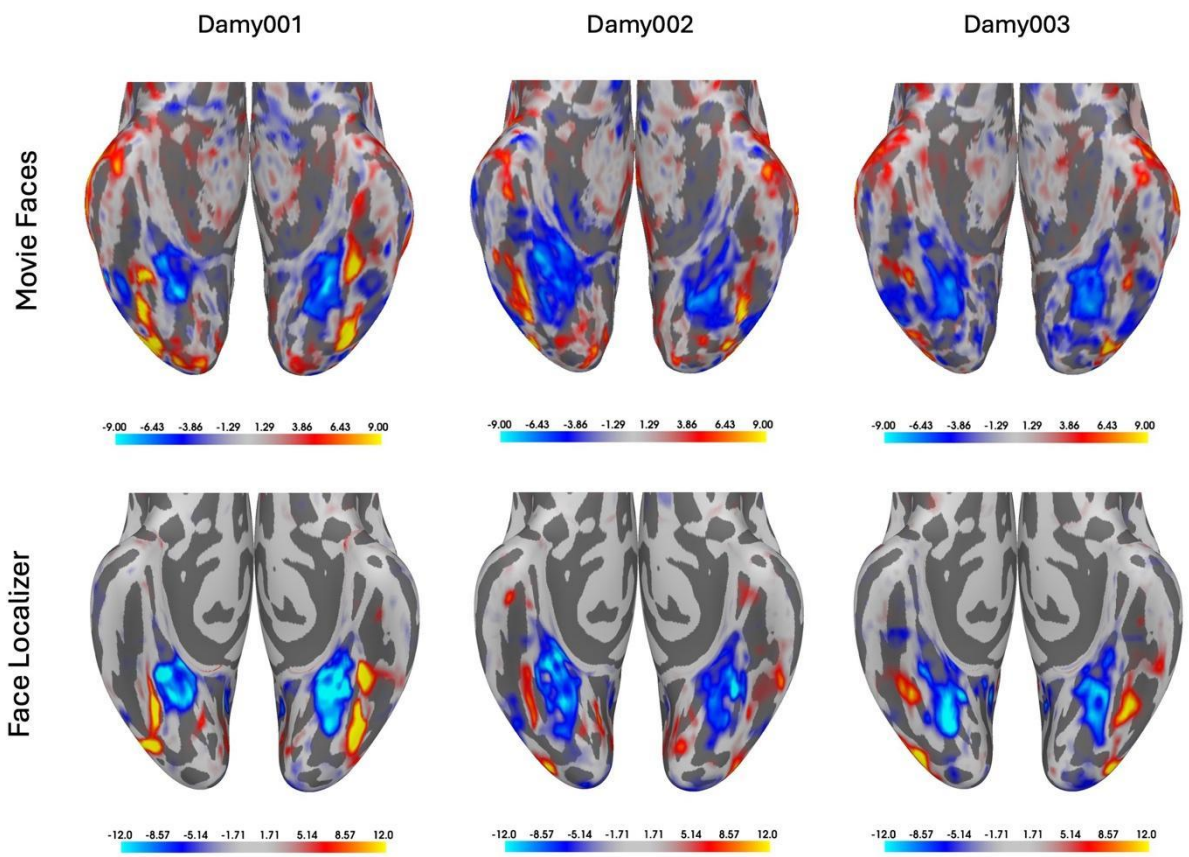

Figure 4: Comparison of univariate modeling of BOLD response to faces in the ventral temporal cortex between a single 15-minute movie segment (budapest1) and a classical face localizer task. The upper row shows the main effect of total face area within a movie frame for each participant. The lower row shows the equivalent faces-shapes contrast in a conventional face localizer task. Both intra-subject similarity and individual differences are evident, particularly in the location and interhemispheric asymmetry of face-responsive patches in the fusiform gyrus (orange-yellow), and in the extent of deactivation in the parahippocampal gyrus (blue-cyan).

fMRI Quality Metrics

Temporal Signal-to-Fluctuation Noise Ratio and Signal Dropout

Temporal signal-to-fluctuation noise ratio (tSFNR) maps[54] were calculated for all 4D BOLD images following quadratic temporal detrending using the *nipype* TSNR module. Dropout was estimated using Equation 1. Voxel-wise means of tSNFR and dropout over all task runs were calculated for each participant in individual template space, allowing the use of Freesurfer tissue labels for extraction of tSFNR and dropout distributions within the amygdala, hippocampus, basal ganglia and cortical gray matter ribbon (Figure 5a).An additional slab-edge mask was imposed on the tissue labels, to exclude signal more than 3 mm above or below the superior-inferior limits of the amygdala label, preventing inclusion of signal from the slab edges which would otherwise overestimate dropout and underestimate tSFNR in the body of the slab. Subcortical median tSFNR varied from approximately 15 to 30, compared to approximately 30 within cortical gray matter (Figure 5b). For comparison to other studies, the volume normalized tSFNR efficiency was calculated from Equation 2

$$\eta_V = tSFNR/V\sqrt{TR} \quad (2)$$

where V is the voxel volume in µl and the repetition time, TR is in seconds. For a voxel volume of 8 µl and TR of 0.556 seconds, regional median η_V varied from approximately 2.5 to 5.0 in subcortex, which compares well with the whole-brain values of approximately 2.75 observed in a larger scale fMRI study by our group using 2.5 mm, 0.7 s TR multiband imaging[57]. Regional signal dropout was almost zero in the hippocampus and showed the greatest inter-individual variation in the amygdala, with distribution median/UQ ranging from approximately 0.0/0.0 (Damy001) to 0.1/0.35 (Damy002) (Figure 5c).

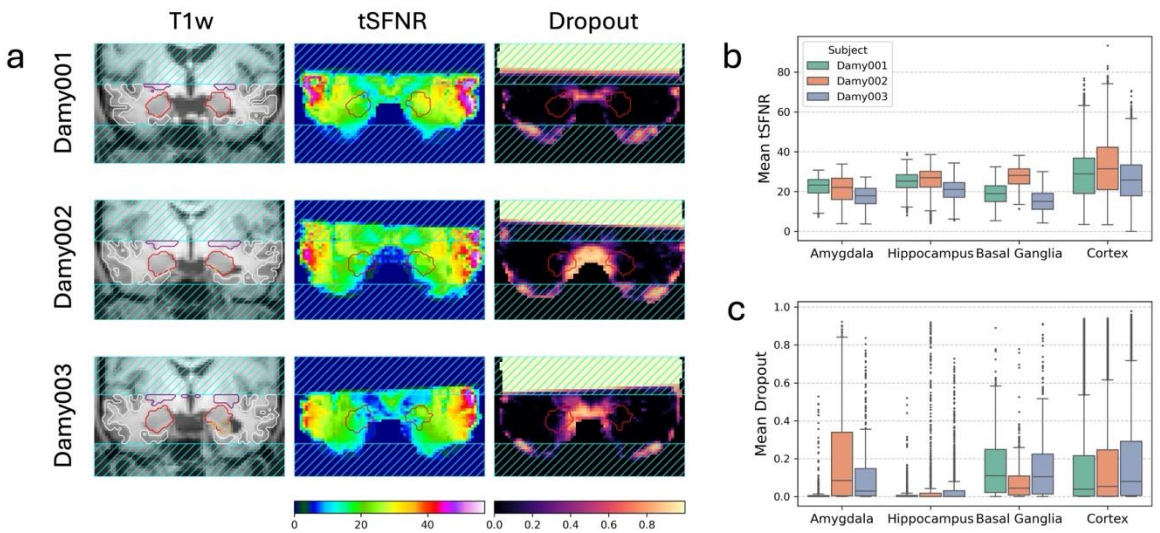

Figure 5: *Regional statistics for the distributions of mean tSFNR and signal dropout over all task runs for each participant. (a) Mid-amygdala coronal sections through T1w anatomy, tSFNR and signal dropout maps. Individual Freesurfer tissue labels for cortical gray matter, amygdala,*

hippocampus and basal ganglia are shown as white, red, green and purple overlays respectively on the T1w section. Brain regions excluded by the slab-edge mask are shown with a light blue hatching. Temporal SFNR maps show an expected exterior to interior gradient with distance from receive coil elements. Medial signal dropout associated with the nasal airspaces shows substantial variation and involvement with the amygdala between individuals. (b) tSFNR in subcortical regions is comparable between subcortical regions with some individual variation. (c) Signal dropout in the amygdala displays a high inter-individual variation, ranging from almost absent (Damy001) to moderate (Damy002, median ~0.1, UQ ~0.35)

Head Motion

Rigid body head motion was summarized using the framewise displacement (FD)[58] timeseries generated by the MRIQC quality control package[59]. FD was additionally low pass filtered (LPF) (Butterworth filter, order 5, f < 0.2 Hz) which minimizes high frequency respiratory contamination in FD timeseries[60,61]. FD and LPF FD distributions (Figure 6a and b) showed median FDs over all sessions and tasks of between 0.12 and 0.14 mm and 99th percentile FDs between 0.54 and 0.67 mm. Following low pass filtering, the median LPF FDs increased slightly to between 0.13 to 0.15 mm with 99th percentile LPF FDs dropping to between 0.37 and 0.43 mm.

Effective Voxel Resolution

The full-width half-maximum (FWHM) isotropic spatial resolution was estimated from spatial noise autocorrelation using AFNI (3dFWHMx)[62]. T2*w EPI time series were demeaned and detrended temporally prior to FWHM estimation. Following single-shot resampling from the raw, distorted EPI space to the undistorted, motion corrected template space, median FWHM for each participant ranged from approximately 2.25 to 2.40 mm (Figure 6c).

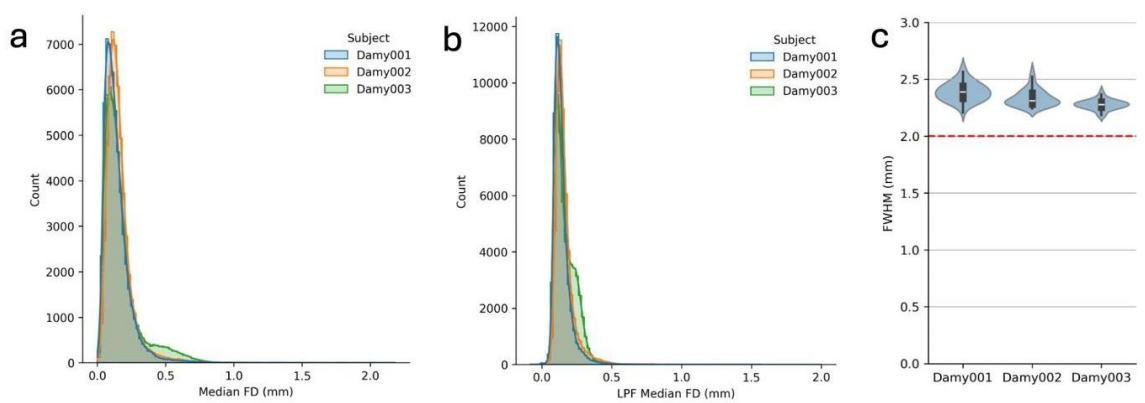

Figure 6: *Head motion estimates. Framewise displacement distributions for each participant (a) before and (b) after low pass temporal filtering. (c) Comparison of FWHM isotropic spatial resolution of the BOLD EPI timeseries following resampling to individual template space. FWHM was estimated by spatiotemporal noise correlation. All participants' data showed a moderate 10%*

to 20% increase in FWHM following one-shot resampling compared to the nominal 2.0 mm voxel size (red dotted line).

Inter-rater Agreement and Consistency for Physiological Denoising

Physiology denoising was performed using the ICA-FIX algorithm trained on manual classifications of a subset of ICA results for the BOLD EPI task series. Inter-rater agreement was assessed using Cohen's Kappa for all rater pairs over all possible classifications and for the binary classification between neurovascular (keep) and non-neurovascular (discard) ICs (Figure 7).

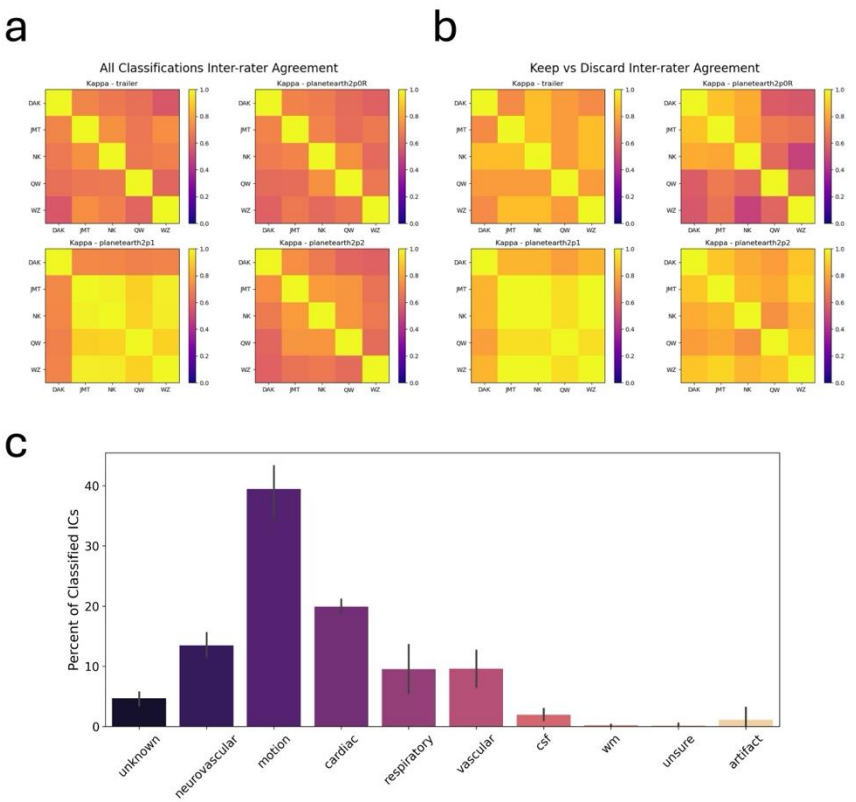

Figure 7: *Inter-rater ICA-FIX training set classification consistency visualized as Cohen's Kappa matrices for all classifications (a) and the keep (neurovascular) vs discard (non-neurovascular) classification over all rated independent components. (c) IC classifications were dominated by gross motion and cardiorespiratory components. The trained ICA-FIX classifier was used to remove non-neurovascular components from the BOLD timeseries. Both the cleaned BOLD timeseries and ICA-FIX classifier are provided in this data release.*

Pupillometry Data Quality

The quality of pupil size data was assessed in two ways. First, the percentage of missing data was calculated for each participant. Second, blinks were automatically detected and extracted from the raw pupil size traces using the *pypillometry* Python package (version 1.0.3.4) . Blinks were

identified with the function *blinks_detect* using the package's '*zero'* strategy, which treats any contiguous run of samples with pupil value equals the missing-data code (0) as a blink. Events shorter than 20 ms or longer than 500 ms were discarded to exclude spurious short drops in pupil size and prolonged signal dropouts. The resulting blink on- and offset timestamps were then used to compute blink-rate, mean blink duration, and inter-blink interval (IBI) for each participant and movie run.

Across all 44 movie runs, the mean proportion of missing data was 5% ± 4.1% (mean ± std), 3.3% ± 2.4%, and 1.7% ± 1.1% for participants Damy001, Damy002, and Damy003, respectively. Mean blink rates were 37.7 ± 20.3, 15.5 ± 8.0, and 12.6 ± 4.1 blinks per minute; mean inter-blink intervals were 1.75 ± 0.38, 4.84 ± 2.30, and 5.29 ± 1.92 seconds; and mean blink durations were 74 ± 9, 114 ± 18, and 83 ± 21 milliseconds, respectively. These values fall within the ranges reported in previous studies of spontaneous blinking during naturalistic movie viewing in fMRI settings, supporting the reliability of the released pupil size data for downstream physiological and cognitive analyses[1].

The released pupil measurements are raw eye-camera estimates and can be affected by eyelid occlusion, blinks, and off-axis gaze (pupil foreshortening), as well as illumination-related segmentation variability. Because gaze position traces are not included in this release, pupil analyses cannot directly correct for gaze-angle–dependent foreshortening. We therefore recommend focusing on within-run relative pupil fluctuations after blink removal/interpolation and detrending and performing additional quality control to exclude prolonged dropouts or abrupt step changes that may reflect partial occlusion or tracking loss.

Usage Notes

This dataset represents an extremely small sample of healthy adults in the spirit of precision functional mapping and is not intended to support broad generalization, as might be the case for large-scale datasets such as the HCP Young Adult, ABCD or OASIS releases. The participants' age range (25-59 years) and psychological deep phenotyping differences may limit interpretability of individual variations if the dataset is used in isolation. However, the amount of data acquired here for each participant greatly exceeds that typically acquired in large-scale cross-sectional studies, allowing for deeper characterization of more subtle individual effects which may not be detected at the group level[3]. The complex-valued fMRI data together with extensive other data types are intended to provide a testbed for movie-fMRI analyses, in particular ones focused on social neuroscience studies of the amygdala. Our aim with this dataset is to improve estimates of BOLD response effect size in individuals that in turn informs prospective experimental designs in larger-scale cross-sectional or precision experiments.

This dataset includes dense, high spatial-resolution, complex-valued BOLD fMRI for comparison with the existing Study Forrest and Grand Budapest Hotel data releases. The documentary films that are unique to our study provide an opportunity for further exploration of social and emotional responses to animal and non-scripted human interactions. We note here that participants found some of the manual emotion feature ratings described above in Video Feature Labeling at times conceptually problematic; for instance, sentimental epochs in a movie were sometimes judged to

have high values on both positive and negative valence, reflected in rapid switching between large positive and large negative values on the rating scale. Users may wish to consider that such epochs likely reflect moments where a unidimensional valence scale inadequately captures mixed emotional states, and that the absolute magnitude of valence ratings in these periods may be more informative as a measure of emotional intensity than as a measure of valence direction.

The 5-minute movie trailer and movie segment repeats allow characterization of test-retest reliability and explained variance in high temporal resolution complex-valued data. Low-level audiovisual feature and physiological waveform time series are provided to allow better control for early audiovisual system effects and physiological confounds in the BOLD response. We also note here that the exclusion from the dataset of gaze estimates due to low accuracy will limit any modeling of overt attention.

Movie-viewing fMRI data were acquired with a TR of 556 ms (sampling rate ~1.80 Hz; Nyquist frequency ~0.9 Hz), enabling characterization of BOLD time-series fluctuations up to ~0.9 Hz in principle (noting that the measured spectrum reflects combined hemodynamic, physiological, and acquisition-related contributions). In our dataset, this sampling rate supports separation of respiratory-related fluctuations (typically ~0.1–0.3 Hz) from aliased cardiac-related components, which appear in the sub-Nyquist band (e.g., ~0.4–0.7 Hz in the tcsICA spectra) rather than folding into the lowest frequencies. However, as with all BOLD fMRI, higher-frequency BOLD fluctuations remain susceptible to physiological contamination and to aliasing of signals above Nyquist; therefore, frequency-specific interpretations should be evaluated cautiously using appropriate denoising and validation strategies (e.g., the provided physiological recordings and ICA-based denoising). Recent reviews emphasize that TR and scan duration jointly determine the measurable frequency range and resolution and should be considered explicitly when defining frequency bands for analysis[63].

The phase channel images (*part-phasediff* images in the OpenNeuro dataset) are dominated by respiration[64] but may contain lower amplitude spatiotemporal signal arising from neurovascular or physiological sources and can be analyzed independently of the magnitude channel or as part of a full complex-valued signal model. A variety of analyses have been proposed for complex-valued resting-state and task fMRI, including complex-valued ICA[65] and its spatial source phase extension[66] and phase-only fMRI[67], all of which could be applied to this dataset. In addition to functional analysis, we note that the phase channel of the 4D BOLD fMRI data could potentially be combined with B_0 fieldmap estimates from the complex-valued spin echo EPI pairs provided for each task run to allow dynamic, per-volume distortion corrections using an approach similar to the REFILL method[68]. Finally, the phase channel encodes local susceptibility variations in brain tissue, enabling functional susceptibility mapping with complementary information to magnitude BOLD fMRI[69,70].

Finally, we note that BOLD fMRI of the medial temporal lobe, including the amygdala has specific challenges compared to superficial cortical fMRI that should be accounted for in any subsequent analysis. The area suffers from lower SNR intrinsically due to distance from receive coil elements and increased noise amplification when using in-plane acceleration[71] and physiological confound signals from neighboring arteries (see for example Figure 3b) and the basal vein of Rosenthal[72] complicate interpretation. It is important to employ accurate tissue segmentation when studying

the amygdala and we provide Freesurfer[50] and CIT168 probabilistic amygdala labels[73] with the dataset, with the understanding that alternative, potentially more accurate segmentations are under constant development[74].

Data Availability

This dataset is made available under a Creative Commons Zero (CC0) license through the OpenNeuro data sharing platform as ds006947[55].

Code Availability

Video presentation scripts implemented in *PsychoPy 2021.2.3*:
https://github.com/adolphslab/DenseAmygdalaRelease

slabpreproc slab-selective EPI preprocessing pipeline implemented in *nipype:*
https://github.com/adolphslab/slabpreproc

PhaseRespWave class for respiratory waveform estimation from temporally unwrapped EPI phase channel images: https://github.com/adolphslab/mriphysio

voxface irreversible deidentification of the face region in structural MRI data:
https://github.com/jmtyszka/voxface

Author Contributions

R.A. and J.M.T. conceived the study. J.M.T., Y.X., and R.A. developed the methodology. J.M.T., U.K., and Z.D. developed the software and performed validation. Formal analysis was conducted by J.M.T., U.K., Z.D., N.K., W.Z., Q.W., and D.A.K. J.M.T. carried out the investigation and provided resources. J.M.T. and Z.D. curated the data. J.M.T., R.A., Z.D., and U.K. wrote the original draft and contributed to review and editing. J.M.T., U.K., and Z.D. produced the visualizations. R.A. and J.M.T. supervised the project, managed project administration, and acquired funding.

Competing Interests

The author(s) declare no competing interests.

Acknowledgements

We are greatly indebted to Dr. Lynn K. Paul for all her help administering and reviewing the session questionnaires in Qualtrics.

Funding

This work was funded by a 2022 Research Grant Award from the T&C Chen Center for Social and Decision Neuroscience at Caltech (JMT and RA).

References

1. Finn, E. S. & Bandettini, P. A. Movie-watching outperforms rest for functional connectivity-based prediction of behavior. *Neuroimage* **235**, 117963 (2021).

2. Finn, E. S. Is it time to put rest to rest? *Trends Cogn. Sci.* (2021) doi:10.1016/j.tics.2021.09.005.

3. Gordon, E. M. *et al.* Precision Functional Mapping of Individual Human Brains. *Neuron* (2017) doi:10.1016/j.neuron.2017.07.011.

4. Fedorenko, E. The early origins and the growing popularity of the individual-subject analytic approach in human neuroscience. *Current Opinion in Behavioral Sciences* **40**, 105–112 (2021).

5. Naselaris, T., Allen, E. & Kay, K. Extensive sampling for complete models of individual brains. *Current Opinion in Behavioral Sciences* **40**, 45–51 (2021).

6. Poldrack, R. A. *et al.* Long-term neural and physiological phenotyping of a single human. *Nat. Commun.* **6**, 8885 (2015).

7. Adolphs, R. What does the amygdala contribute to social cognition? - Adolphs - 2010 - Annals of the New York Academy of Sciences - Wiley Online Library. *Ann. N. Y. Acad. Sci.* (2010) doi:10.1111/j.1749-6632.2010.05445.x/pdf.

8. Varkevisser, T., Geuze, E. & van Honk, J. Amygdala fMRI-A critical appraisal of the extant literature. *Neurosci. Insights* **19**, 26331055241270591 (2024).

9. West, H. V., Burgess, G. C., Dust, J., Kandala, S. & Barch, D. M. Amygdala activation in cognitive task fMRI varies with individual differences in cognitive traits. *Cogn. Affect. Behav. Neurosci.* **21**, 254–264 (2021).

10. Canli, T., Sivers, H., Whitfield, S. L., Gotlib, I. H. & Gabrieli, J. D. E. Amygdala response to happy faces as a function of extraversion. *Science* **296**, 2191 (2002).

11. Byrge, L. *et al.* Video-evoked fMRI BOLD responses are highly consistent across different data acquisition sites. *Hum. Brain Mapp.* (2022) doi:10.1002/hbm.25830.

12. Meer, J. N. van der, Breakspear, M., Chang, L. J., Sonkusare, S. & Cocchi, L. Movie viewing elicits rich and reliable brain state dynamics. *Nat. Commun.* **11**, 5004 (2020).

13. Sonkusare, S., Breakspear, M. & Guo, C. Naturalistic stimuli in neuroscience: Critically acclaimed. *Trends Cogn. Sci.* **23**, 699–714 (2019).

14. Vanderwal, T., Eilbott, J. & Castellanos, F. X. Movies in the magnet: Naturalistic paradigms in developmental functional neuroimaging. *Dev. Cogn. Neurosci.* **36**, 100600 (2019).

15. Saarimäki, H. Naturalistic Stimuli in Affective Neuroimaging: A Review. *Front. Hum. Neurosci.* **15**, 675068 (2021).

16. Hanke, M. *et al.* A high-resolution 7-Tesla fMRI dataset from complex natural stimulation with an audio movie. *Sci Data* **1**, 140003 (2014).

17. Visconti di Oleggio Castello, M., Chauhan, V., Jiahui, G. & Gobbini, M. I. An fMRI dataset in response to "The Grand Budapest Hotel", a socially-rich, naturalistic movie. *Sci Data* **7**, 383 (2020).

18. Morgenroth, E. *et al.* Emo-FilM: A multimodal dataset for affective neuroscience using naturalistic stimuli. *Sci. Data* **12**, 684 (2025).

19. Aliko, S., Huang, J., Gheorghiu, F., Meliss, S. & Skipper, J. I. A naturalistic neuroimaging database for understanding the brain using ecological stimuli. *Sci Data* **7**, 347 (2020).

20. Poldrack, R. A. Precision neuroscience: Dense sampling of individual brains. *Neuron* **95**, 727–729 (2017).

21. Hanke, M. *et al.* A studyforrest extension, simultaneous fMRI and eye gaze recordings during prolonged natural stimulation. *Sci Data* **3**, 160092 (2016).

22. Agtzidis, I., Meyhöfer, I., Dorr, M. & Lencer, R. Following Forrest Gump: Smooth pursuit related brain activation during free movie viewing. *Neuroimage* **216**, 116491 (2020).

23. Jiahui, G. *et al.* Predicting individual face-selective topography using naturalistic stimuli. *Neuroimage* **216**, 116458 (2020).

24. Jiahui, G. *et al.* Modeling naturalistic face processing in humans with deep convolutional neural networks. *Proc. Natl. Acad. Sci. U. S. A.* **120**, e2304085120 (2023).

25. Bernal-Rusiel, J. L. *et al.* Statistical analysis of longitudinal neuroimage data with Linear Mixed Effects models. *Neuroimage* **66**, 249–260 (2013).

26. Esteban, O. *et al.* fMRIPrep: a robust preprocessing pipeline for functional MRI. *Nat. Methods* **16**, 111–116 (2019).

27. Esteban, O., Markiewicz, C. J. & Goncalves, M. *SDCflows: Susceptibility Distortion Correction workFLOWS*. (Zenodo, 2024). doi:10.5281/ZENODO.12654387.

28. Drew, P. J. Vascular and neural basis of the BOLD signal. *Curr. Opin. Neurobiol.* **58**, 61–69 (2019).

29. Hillman, E. M. C. Coupling mechanism and significance of the BOLD signal: a status report. *Annu. Rev. Neurosci.* **37**, 161–181 (2014).

30. Epp, S. M. *et al.* BOLD signal changes can oppose oxygen metabolism across the human cortex. *Nat. Neurosci.* 1–12 (2025) doi:10.1038/s41593-025-02132-9.

31. Visconti di Oleggio Castello, M., Haxby, J. V. & Gobbini, M. I. Shared neural codes for visual and semantic information about familiar faces in a common representational space. *Proc. Natl. Acad. Sci. U. S. A.* **118**, e2110474118 (2021).

32. Chen, J., Papies, E. K. & Barsalou, L. W. A core eating network and its modulations underlie diverse eating phenomena. *Brain Cogn.* **110**, 20–42 (2016).

33. Sato, W., Kochiyama, T., Minemoto, K., Sawada, R. & Fushiki, T. Amygdala activation during unconscious visual processing of food. *Sci. Rep.* **9**, 7277 (2019).

34. Douglass, A. M. *et al.* Central amygdala circuits modulate food consumption through a positive-valence mechanism. *Nat. Neurosci.* **20**, 1384–1394 (2017).

35. Mormann, F. *et al.* A category-specific response to animals in the right human amygdala. *Nat. Neurosci.* **14**, 1247–1249 (2011).

36. Psychtoolbox-3. http://psychtoolbox.org/.

37. StudyForrest Project. studyforrest.org. https://studyforrest.org/.

38. A. Everything Everywhere All At Once | Official Trailer HD | A24. https://www.youtube.com/watch?v=wxN1T1uxQ2g (2021).

39. Films, S. G. Big Gold Brick - Official Trailer. https://www.youtube.com/watch?v=uDoQ2qzO8Rw (2021).

40. Movies, L. Warning (2021 Movie) Official Trailer - Thomas Jane, Alex Pettyfer, Alice Eve. https://www.youtube.com/watch?v=H9Cpdh0eKuc (2021).

41. The FFmpeg Developer Team. FFmpeg - A complete, cross-platform solution to record, convert and stream audio and video. https://ffmpeg.org/ (2023).

42. Beck, A. T., Steer, R. A. & Brown, G. K. *BDI-II, Beck Depression Inventory: Manual*. (Psychological Corporation, 1996).

43. Spielberger, C. D., Gorsuch, R. L., Lushene, R., Vagg, P. R. & Jacobs, G. A. *STAI: Manual for the State-Trait Anxiety Inventory*. (1983).

44. Watson, D., Clark, L. A. & Tellegen, A. Development and validation of brief measures of positive and negative affect: the PANAS scales. *J. Pers. Soc. Psychol.* **54**, 1063–1070 (1988).

45. Cohen, S., Kamarck, T. & Mermelstein, R. A Global Measure of Perceived Stress. *J. Health Soc. Behav.* **24**, 385–396 (1983).

46. Cohen, S. & Janicki-Deverts, D. Who's stressed? Distributions of psychological stress in the United States in probability samples from 1983, 2006, and 20091. *J. Appl. Soc. Psychol.* **42**, 1320–1334 (2012).

47. *Insightface: State-of-the-Art 2D and 3D Face Analysis Project*. (Github).

48. Avants, B. B., Duda, J. T., Zhang, H. & Gee, J. C. Multivariate normalization with symmetric diffeomorphisms for multivariate studies. *Med. Image Comput. Comput. Assist. Interv.* **10**, 359–366 (2007).

49. Brian B Avants, Nicholas J. Tustison, Hans J. Johnson. Advanced Normalization Tools (ANTs). https://github.com/ANTsX/ANTs (2014).

50. Fischl, B. FreeSurfer. *Neuroimage* **62**, 774–781 (2012).

51. Ségonne, F., Pacheco, J. & Fischl, B. Geometrically accurate topology-correction of cortical surfaces using nonseparating loops. *IEEE Trans. Med. Imaging* **26**, 518–529 (2007).

52. Gorgolewski, K. *et al.* Nipype: a flexible, lightweight and extensible neuroimaging data processing framework in python. *Front. Neuroinform.* **5**, 13 (2011).

53. Glasser, M. F. *et al.* The minimal preprocessing pipelines for the Human Connectome Project. *Neuroimage* **80**, 105–124 (2013).

54. Friedman, L., Glover, G. H. & Fbirn Consortium. Reducing interscanner variability of activation in a multicenter fMRI study: controlling for signal-to-fluctuation-noise-ratio (SFNR) differences. *Neuroimage* **33**, 471–481 (2006).

55. Tyszka, J. M. *et al.* OpenNeuro ds006947. *Dense complex-valued partial brain BOLD of passive audiovisual movie presentations* https://doi.org/10.18112/openneuro.ds006947.v1.0.1 (2026).

56. Beckmann, C. F. & Smith, S. M. Probabilistic independent component analysis for functional magnetic resonance imaging. *IEEE Trans. Med. Imaging* **23**, 137–152 (2004).

57. Kliemann, D. *et al.* Caltech Conte Center, a multimodal data resource for exploring social cognition and decision-making. *Scientific Data* **9**, 1–15 (2022).

58. Power, J. D., Barnes, K. A., Snyder, A. Z., Schlaggar, B. L. & Petersen, S. E. Spurious but systematic correlations in functional connectivity MRI networks arise from subject motion. *Neuroimage* **59**, 2142–2154 (2012).

59. Esteban, O. *et al.* MRIQC: Advancing the automatic prediction of image quality in MRI from unseen sites. *PLoS One* **12**, e0184661 (2017).

60. Power, J. D. *et al.* Distinctions among real and apparent respiratory motions in human fMRI data. *Neuroimage* **201**, 116041 (2019).

61. Gratton, C. *et al.* Removal of high frequency contamination from motion estimates in single-band fMRI saves data without biasing functional connectivity. *Neuroimage* 116866 (2020) doi:10.1016/j.neuroimage.2020.116866.

62. Cox, R. W., Chen, G., Glen, D. R., Reynolds, R. C. & Taylor, P. A. FMRI Clustering in AFNI: False-Positive Rates Redux. *Brain Connect.* **7**, 152–171 (2017).

63. Gong, Z.-Q. & Zuo, X.-N. Dark brain energy: Toward an integrative model of spontaneous slow oscillations. *Phys. Life Rev.* **52**, 278–297 (2025).

64. Syväoja, S. S. *et al.* Ultrafast complex-valued 4D fMRI reveals sleep-induced brain respiratory pulsation changes in both magnitude and phase signals. *Neuroimage* **317**, 121290 (2025).

65. Yu, M.-C. *et al.* ICA of full complex-valued fMRI data using phase information of spatial maps. *J. Neurosci. Methods* **249**, 75–91 (2015).

66. Qiu, Y. *et al.* Spatial source phase: A new feature for identifying spatial differences based on complex-valued resting-state fMRI data. *Hum. Brain Mapp.* **40**, 2662–2676 (2019).

67. Chen, Z., Fu, Z. & Calhoun, V. Phase fMRI reveals more sparseness and balance of rest brain functional connectivity than magnitude fMRI. *Front. Neurosci.* **13**, 204 (2019).

68. Robinson, S. D. *et al.* Improved dynamic distortion correction for fMRI using single-echo EPI and a readout-reversed first image (REFILL). *Hum. Brain Mapp.* **44**, 5095–5112 (2023).

69. Lancione, M. *et al.* Complementing canonical fMRI with functional Quantitative Susceptibility Mapping (fQSM) in modern neuroimaging research. *Neuroimage* **244**, 118574 (2021).

70. Chen, Z. & Calhoun, V. T2* phase imaging and processing for brain functional magnetic susceptibility (χ) mapping. *Biomed. Phys. Eng. Express* **2**, 025015 (2016).

71. Wiggins, G. C. *et al.* 32-channel 3 Tesla receive-only phased-array head coil with soccer-ball element geometry. *Magn. Reson. Med.* **56**, 216–223 (2006).

72. Boubela, R. N. *et al.* fMRI measurements of amygdala activation are confounded by stimulus correlated signal fluctuation in nearby veins draining distant brain regions. *Sci. Rep.* **5**, 10499 (2015).

73. Tyszka, J. M. & Pauli, W. M. An in vivo atlas of the human amygdala. https://doi.org/DOI%252010.17605/OSF.IO/HKSA6 (2017).

74. Zhou, Q. *et al.* Charting the human amygdala development across childhood and adolescence: Manual and automatic segmentation. *Dev. Cogn. Neurosci.* **52**, 101028 (2021).